
Efficient Near Field Antenna Analysis using Compressive Sensing

M. Salucci, N. Anselmi, and A. Massa

2024/03/29

Contents

1 Test Case 3 : AUT without failures ($\nu^{(s)} \in [0.0, 0.5]$, $F^{(s)} = 7$ and $\gamma^{(s)} \in [0, \frac{\pi}{4}]$, $P^{(s)} = 5$)	3
1.1 Comparison between original (<i>OMP</i>) and alternative (<i>BCS</i>) MbD	7
1.1.1 OMP vs best BCS	10
1.2 Incremented failure ranges to build the over-complete basis ($\nu^{(s)} \in [0.0, 1.0]$, $F^{(s)} = 7$ and $\gamma^{(s)} \in [-\pi, \pi]$, $P^{(s)} = 5$)	15
1.2.1 Comparison between original (<i>OMP</i>) and alternative (<i>BCS</i>) MbD	16
1.2.2 OMP vs best BCS	20

ELEDIA Research Center

1 Test Case 3 : AUT without failures ($\nu^{(s)} \in [0.0, 0.5]$, $F^{(s)} = 7$ and $\gamma^{(s)} \in [0, \frac{\pi}{4}]$, $P^{(s)} = 5$)

Parameters

Gold Antenna (Without Defects)

- Geometry : Planar array of microstrip patches on the (x, y) plane;
- Working Frequency : $f = 3.6 [GHz]$ ($\lambda = 83.27 \times 10^{-3} [m]$ in free space);
- Substrate (PEC-backed) :
 - Dimensions : infinite;
 - Relative Permittivity : $\epsilon_{r,sub} = 4.7$;
 - Loss Tangent : $\tan \delta_{sub} = 0.014$;
 - Thickness : $h_{sub} = 0.019 [\lambda]$ ($1.6 [mm]$);
- Microstrip patches :
 - Dimensions : $l_x \approx 0.22 [\lambda]$ ($18.16 [mm]$), $l_y \approx 0.33 [\lambda]$ ($27.25 [mm]$);
 - Feeding : pin-fed;
- Spacing between elements : $d_x = d_y = \frac{\lambda}{2}$;
- Number of elements in each row : $N_x = 6$;
- Number of elements in each column : $N_y = 10$;
- Total number of elements : $N = (N_x \times N_y) = 60$;
- Total size of the antenna : $L_x = 5 [\lambda]$, $L_y = 9 [\lambda]$;
- Element excitations : $w_n^{(s)} = 1.0 + j0.0$, $n = 1, \dots, N^{(s)}$, $s = 1, \dots, S$;

Antenna Under Test (AUT - With Defects)

In this test case the AUT is set equal to the gold antenna, meaning that the antenna under measurement have no defects.

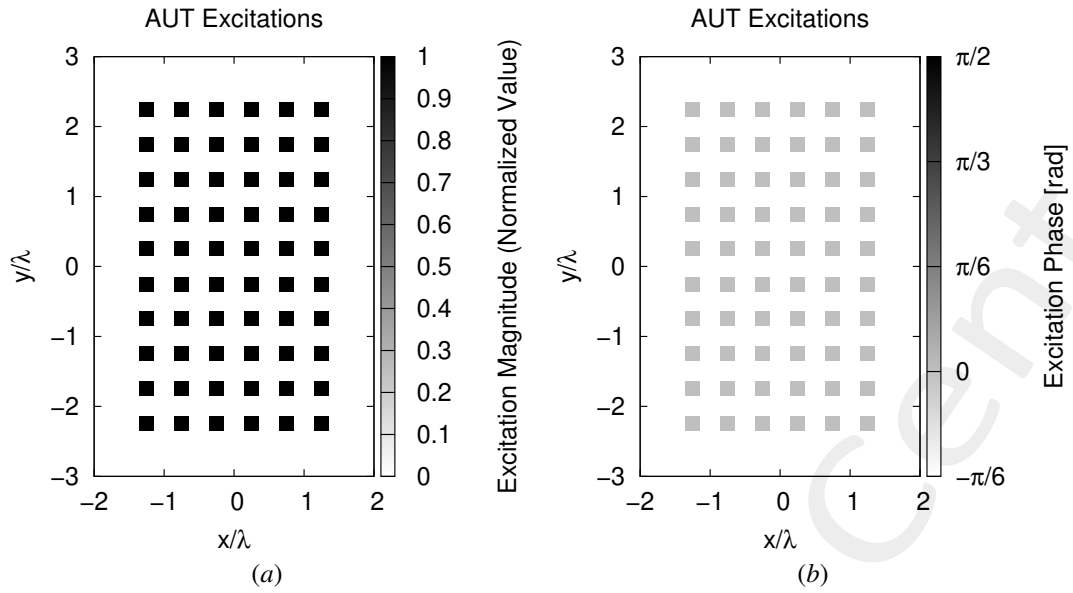


Figure 1: (a) Magnitude of the element excitations in the AUT , (b) phase of the element excitations in the AUT .

Measurement Set-Up

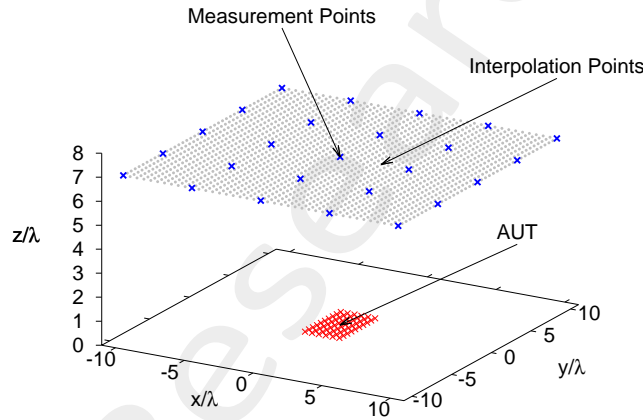


Figure 2: Disposition of the interpolation points ($T = 1681$) and of the measurement points ($M = 25$) in the near-field region of the AUT

- Type of measurements : near-field;
- Height of the measurement region : $H = 7 [\lambda]$;
- Interpolation points :
 - Number of points : $T = 41 \times 41 = 1681$;
 - Coordinates : $x_t \in [-10, 10] [\lambda]$, $y_t \in [-10, 10] [\lambda]$, $z_t = H [\lambda]$, $t = 1, \dots, T$;
 - Interpolation step : $\Delta_{x/y}^{int} = 0.5 [\lambda]$;
- Measurement points :
 - Coordinates : $x_m^{meas} \in [-10, 10] [\lambda]$, $y_m^{meas} \in [-10, 10] [\lambda]$, $z_m^{meas} = H [\lambda]$, $m = 1, \dots, M$;
 - Number of points : $M_{x/y} = 5 \rightarrow M = 25$;

- Measurement step : $\Delta_{x/y}^{meas} = 5 [\lambda]$
- Ratio between number of measurements and total number of elements : $(M/N) = 0.42$;

Measurement-by-Design Technique

- Number of generated bases : $B = 20$;
- Bases $b = 1, \dots, 10$: magnitude failures in each row ($s = 1, \dots, 10$)
 - Failure factor of the elements : $\nu^{(s)} \in [0.0, 0.5]$, $s = 1, \dots, 10$;
 - Number of simulated failure factors : $F^{(s)} = 7$, $s = 1, \dots, 10$;
- Bases $b = 11, \dots, 20$: phase failures in each row ($s = 1, \dots, 10$)
 - Phase shift of the elements : $\gamma^{(s)} \in [0, \frac{\pi}{4}] [rad]$, $s = 1, \dots, 10$;
 - Number of simulated phase shifts: $P^{(s)} = 5$, $s = 1, \dots, 10$;
- Threshold on the singular values magnitude (normalized) : $\eta = -40 [dB]$;
- Total number of simulated *AUT* configurations : $K = S \times (F^{(s)} + P^{(s)}) = 10 \times (7 + 5) = 120$;

Dimension of the Over-Complete Basis

The dimension of the over-complete basis is

$$Q = 40$$

This number is given by the sum of the vectors belonging to the two considered bases:

1. Magnitude failures : $Q_1, \dots, Q_{10} = 2$;
2. Phase failures : $Q_{11}, \dots, Q_{20} = 2$.

Alternative (*BCS*) MbD parameters

- Toleration factor for *BCS* solver: $Tolerance = 1 \times 10^{-8}$;
- Initial noise variance for *BCS* solver: $\eta_0^{opt1} = 10^{-2}$ and $\eta_0^{opt2} = 5 \times 10^{-4}$. This values have been obtained as a result of a calibration procedure;

Original (*OMP*) MbD parameters

- Max. number of iterations of the *OMP* algorithm : $I = \{1; 2; 3; \dots; 10\}$;
- Selected iteration to report the results: $I = 2$; this choice is justified by the fact that at this iteration the *OMP* algorithm reaches the best near field error as shown in the following Fig. 3.

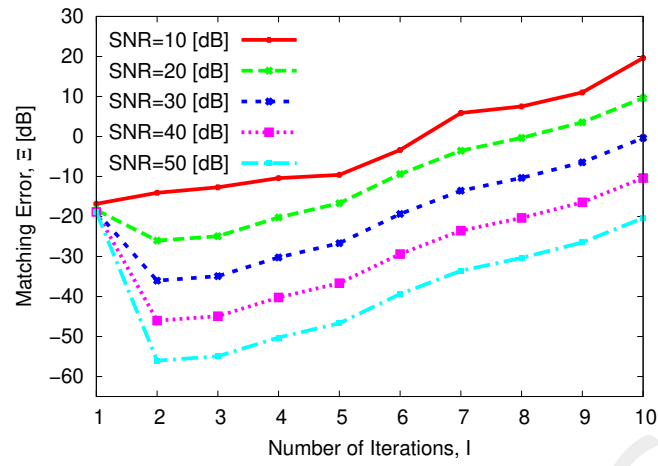


Figure 3: Behaviour of the near-field matching error versus the number of *OMP* iterations, I .

Noise

- *SNR* on the measured data : $SNR = \{50; 40; 30; 20; 10\} [dB]$;
- Noise seed : $Noise_Seed = 11$.

1.1 Comparison between original (*OMP*) and alternative (*BCS*) MbD

Near-Field Error

The comparison, in terms of near field error, between the original (*OMP*) and the alternative (*BCS*) MbD is reported in the following Fig. 4.

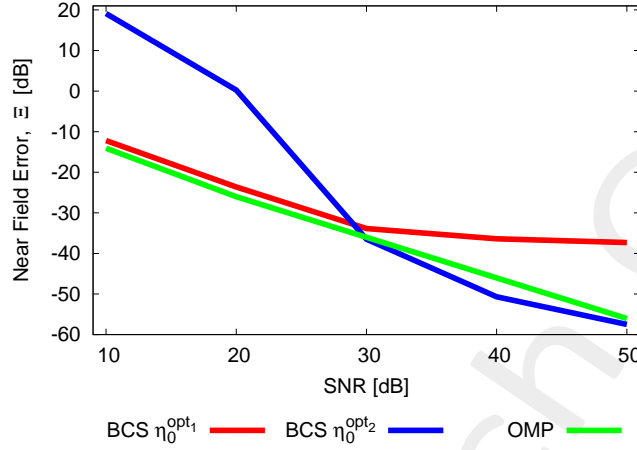


Figure 4: Near Field Error comparison between original (*OMP*) and alternative (*BCS*) MbD for different *SNR* values.

<i>SNR</i> [dB]	Near Field Error, Ξ [dB]		
	<i>BCS</i>		<i>OMP</i>
	$\eta_0^{opt_1}$	$\eta_0^{opt_2}$	
50	-37.32	-57.48	-56.03
40	-36.39	-50.69	-46.03
30	-33.88	-36.48	-36.03
20	-23.62	0.24	-26.03
10	-12.19	19.12	-14.08

Table I: Near Field Errors obtained by the original (*OMP*) and alternative (*BCS*) MbD

Observations

- In this test case, the *OMP* algorithm performs well being able to achieve an error $\Xi < -20$ [dB] already for $SNR = 20$ [dB]. If compared to the *BCS* solver, the *OMP* results are very close to those of the *BCS* with $\eta_0^{opt_1}$ for $SNR \leq 30$ [dB] and of the *BCS* with $\eta_0^{opt_2}$ for $SNR \geq 30$ [dB];
- About the *BCS* algorithm:
 - using $\eta_0^{opt_1}$, the *BCS* solver obtains an error that comparable to that of the *OMP* algorithm for $SNR \leq 30$ [dB] but then its error remains stable while the *OMP* error decreases;
 - using $\eta_0^{opt_2}$, the *BCS* algorithm obtains results which are the worst for $SNR \leq 30$ [dB] but the best, and close to those of the *OMP* algorithm, for $SNR \geq 30$ [dB].

Estimated Near-Field

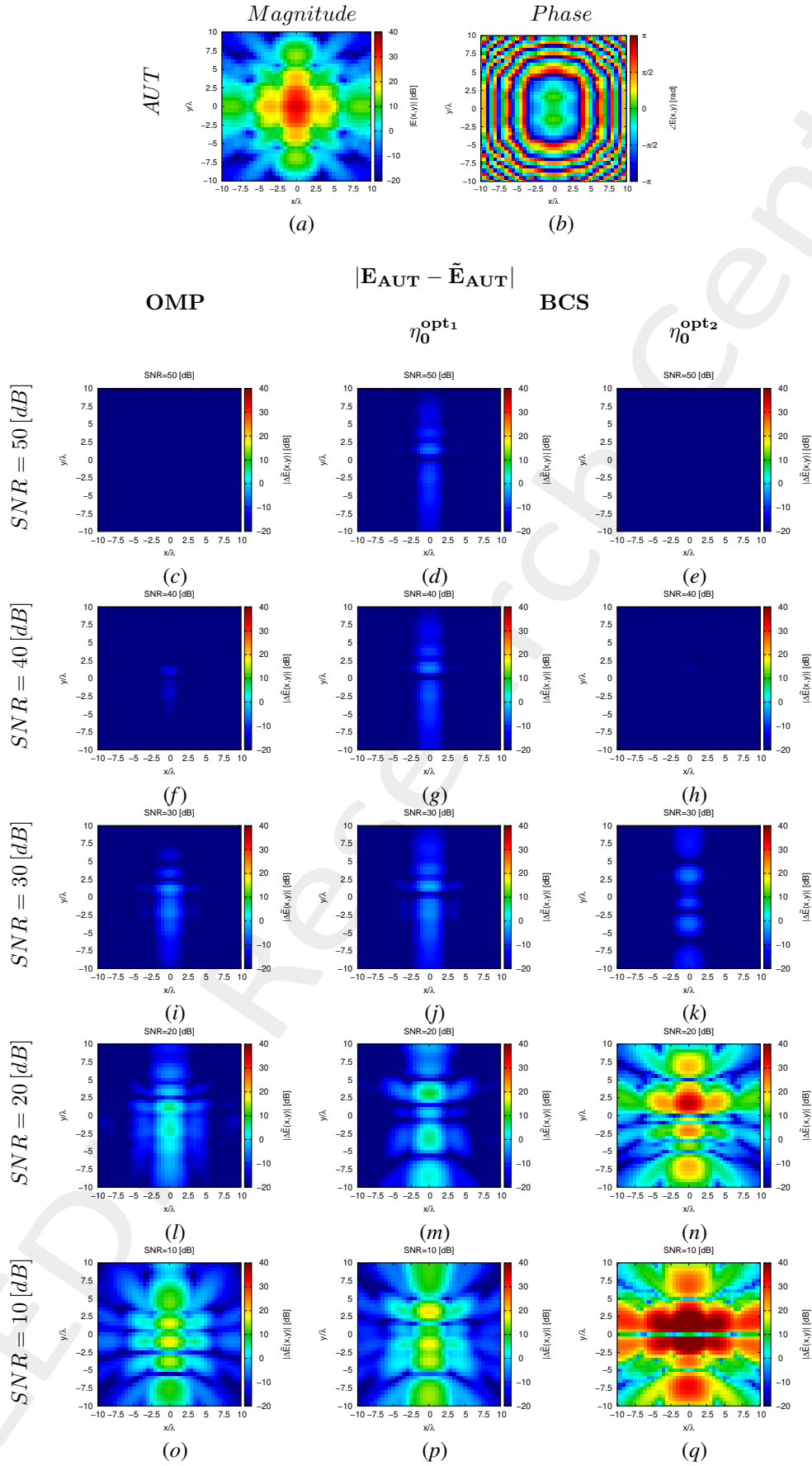


Figure 5: Magnitude difference between the actual and estimated 2 – D near-field pattern when processing noisy measurements at different SNRs.

Estimated Coefficients

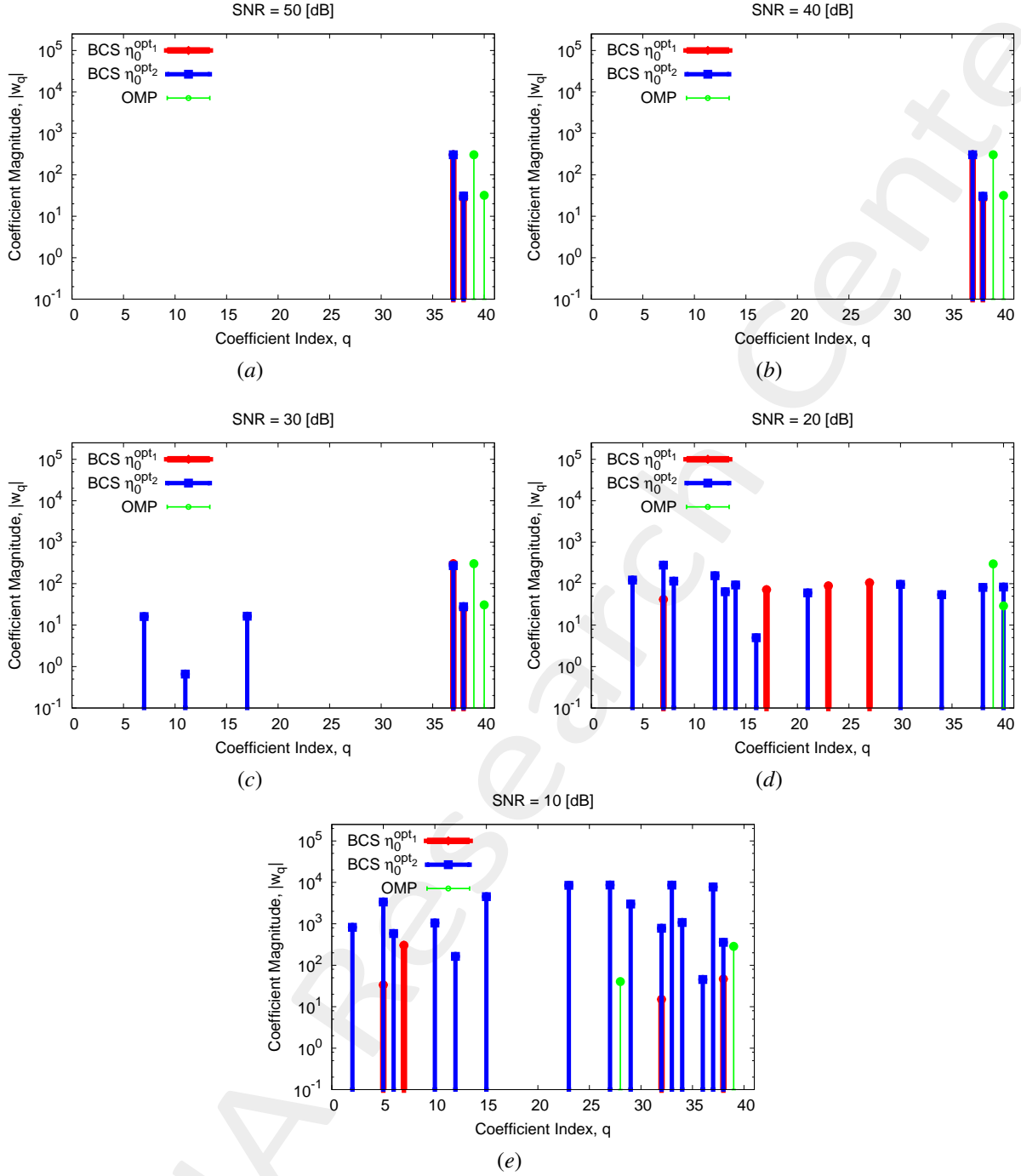


Figure 6: Coefficient comparison between original (*OMP*) and alternative (*BCS*) MbD : (a) $SNR = 50$ [dB], (b) $SNR = 40$ [dB], (c) $SNR = 30$ [dB], (d) $SNR = 20$ [dB], (e) $SNR = 10$ [dB]

Observations

- The *OMP* solver selects always the same vectors (vector indexes $q = 39, 40$) for $SNR \geq 20$ [dB], which are related to phase failures and different from those selected by the *BCS* algorithm;
- The *BCS* algorithm presents solutions that are not sparse for low SNR values, $SNR = 20$ [dB] and $SNR = 10$ [dB], when η_0^{opt2} is used. Both the two *BCS* versions select two same vectors (vector index $q = 37, 38$) obtaining the same solution for $SNR \geq 40$ [dB], solution that is always different from that of the *OMP* solver.

1.1.1 OMP vs best BCS

The main idea of this section is to compare the performance of the *OMP* algorithm and the best *BCS* configuration.

Near-Field Error

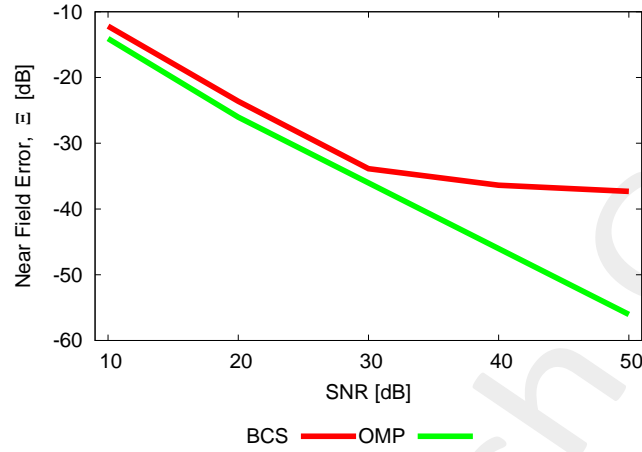


Figure 7: Near Field Error comparison between original (*OMP*) and alternative (*BCS*) MbD for different *SNR* values.

<i>SNR</i> [dB]	Near Field Error, Ξ [dB]	
	<i>BCS</i>	<i>OMP</i>
50	-37.32	-56.03
40	-36.39	-46.03
30	-33.88	-36.03
20	-23.62	-26.03
10	-12.19	-14.08

Table II: Near Field Errors obtained by the original (*OMP*) and alternative (*BCS*) MbD

Estimated Far-Field

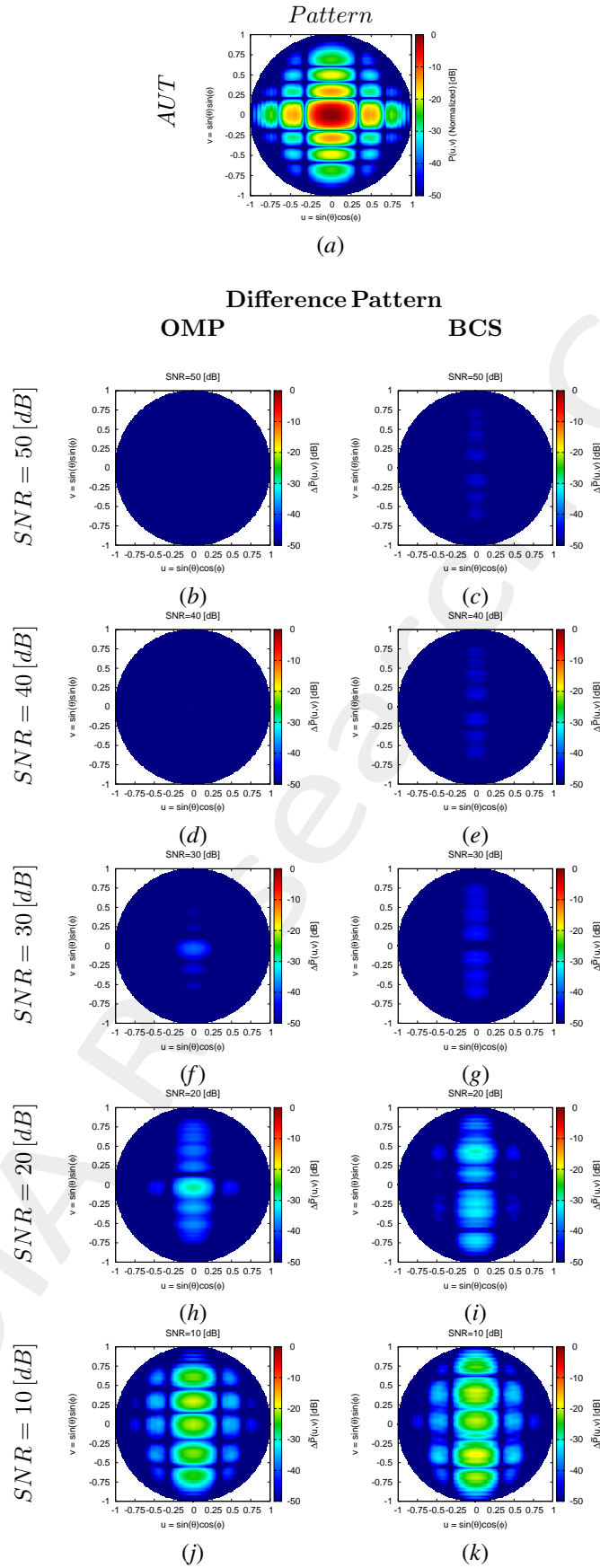


Figure 8: Difference between the actual and estimated 2 – D far-field pattern when processing noisy measurements at different $SNRs$.

Cut @ $v = 0$

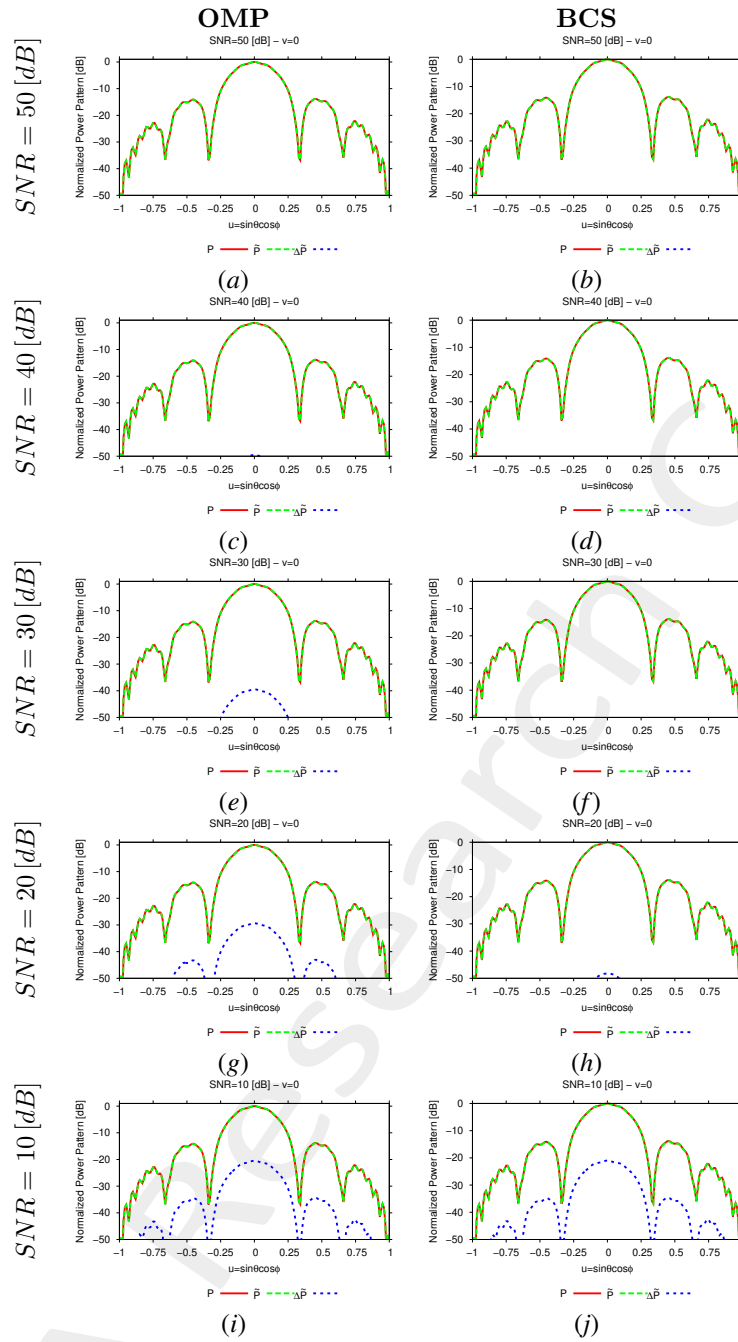


Figure 9: 1 - D cuts of the estimated far-field pattern (obtained through near-to-far-field transformation from the estimated near-field patterns) under several noisy conditions

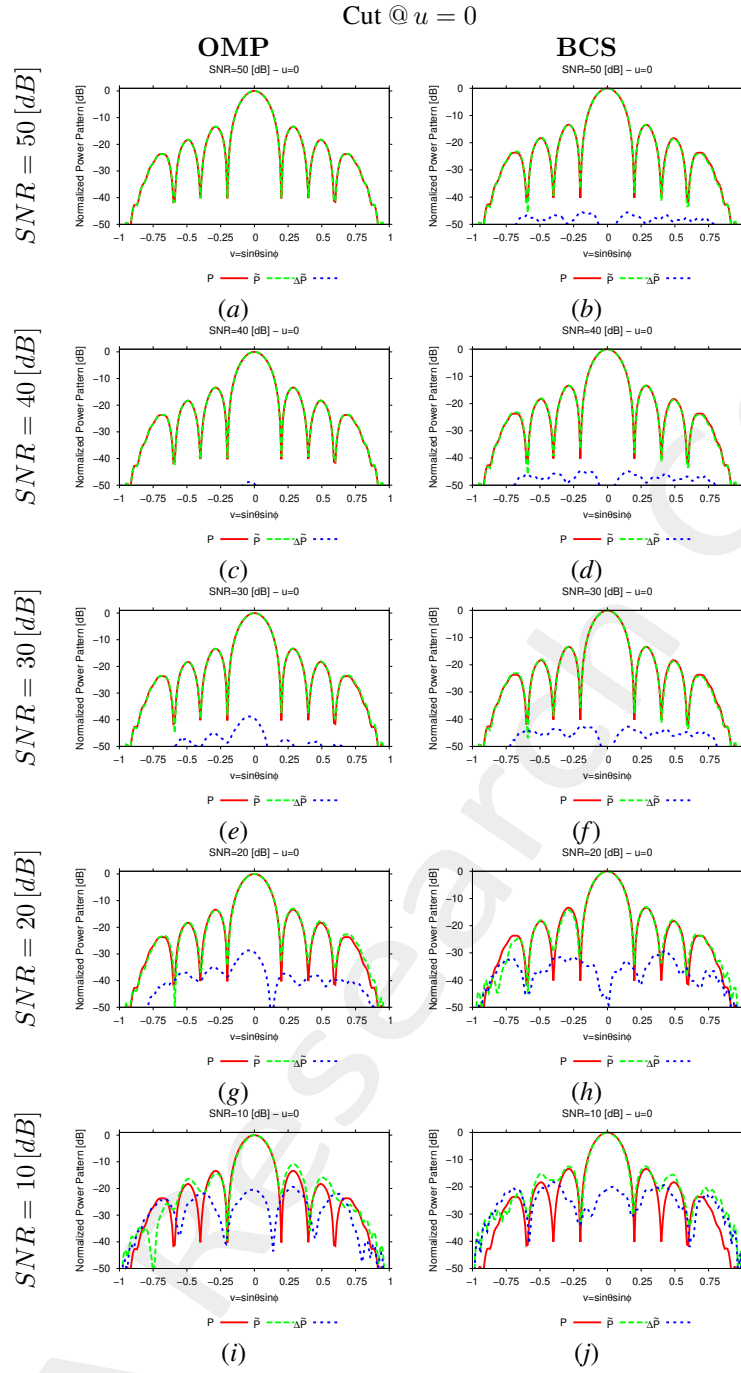


Figure 10: 1 – D cuts of the estimated far-field pattern (obtained through near-to-far-field transformation from the estimated near-field patterns) under several noisy conditions

SNR [dB]	Far – Field Error, χ [dB]	
	BCS	OMP
50	–38.87	–57.17
40	–38.09	–47.16
30	–35.98	–37.13
20	–25.07	–27.03
10	–13.54	–15.23

Table III: Far-field matching error between the actual and estimated AUT patterns (both obtained through near-to-far-field transformation from the corresponding near-field patterns) under several noisy conditions.

Estimated Coefficients

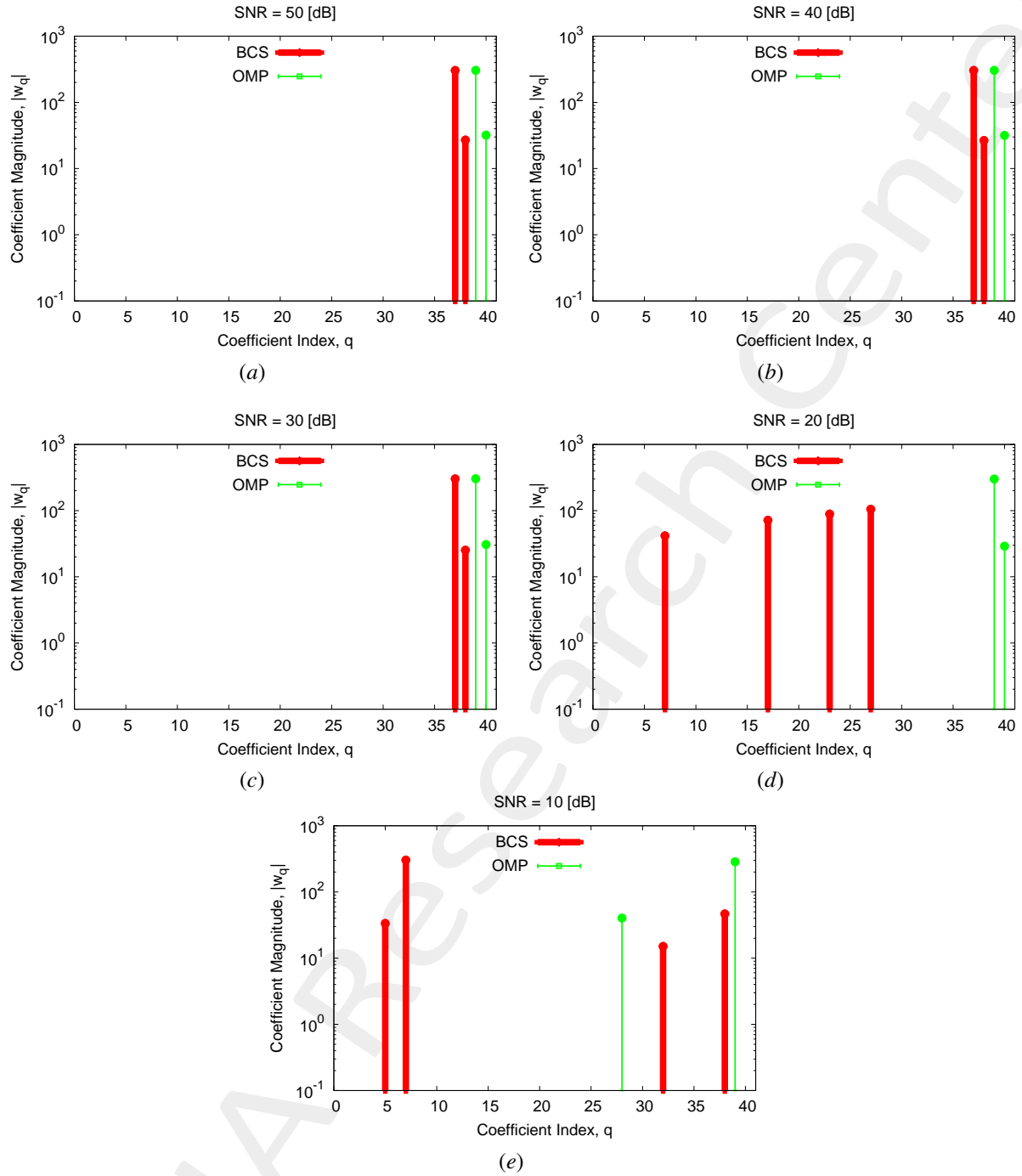


Figure 11: Coefficient comparison between original (*OMP*) and alternative (*BCS*) MbD: (a) $SNR = 50$ [dB], (b) $SNR = 40$ [dB], (c) $SNR = 30$ [dB], (d) $SNR = 20$ [dB], (e) $SNR = 10$ [dB]

1.2 Incremented failure ranges to build the over-complete basis ($\nu^{(s)} \in [0.0, 1.0]$, $F^{(s)} = 7$ and $\gamma^{(s)} \in [-\pi, \pi]$, $P^{(s)} = 5$)

Note: All the simulation parameters are the same of those listed in Sez. 1, except the following ones:

Measurement-by-Design Technique

- Number of generated bases : $B = 20$;
- Bases $b = 1, \dots, 10$: magnitude failures in each row ($s = 1, \dots, 10$)
 - **Failure factor of the elements** : $\nu^{(s)} \in [0.0, 1.0]$, $s = 1, \dots, 10$;
 - Number of simulated failure factors : $F^{(s)} = 7$, $s = 1, \dots, 10$;
- Bases $b = 11, \dots, 20$: phase failures in each row ($s = 1, \dots, 10$)
 - **Phase shift of the elements** : $\gamma^{(s)} \in [-\pi, \pi] [rad]$, $s = 1, \dots, 10$;
 - Number of simulated phase shifts: $P^{(s)} = 5$, $s = 1, \dots, 10$;
- Threshold on the singular values magnitude (normalized) : $\eta = -40 [dB]$;
- Total number of simulated *AUT* configurations : $K = S \times (F^{(s)} + P^{(s)}) = 10 \times (7 + 5) = 120$;

Original (*OMP*) MbD parameters

- Max. number of iterations of the *OMP* algorithm : $I = \{1; 2; 3; \dots; 10\}$;
- Selected iteration to report the results: $I = 2$; this choice is justified by the fact that at this iteration the *OMP* algorithm reaches the best near field error as shown in the following Fig. 12.

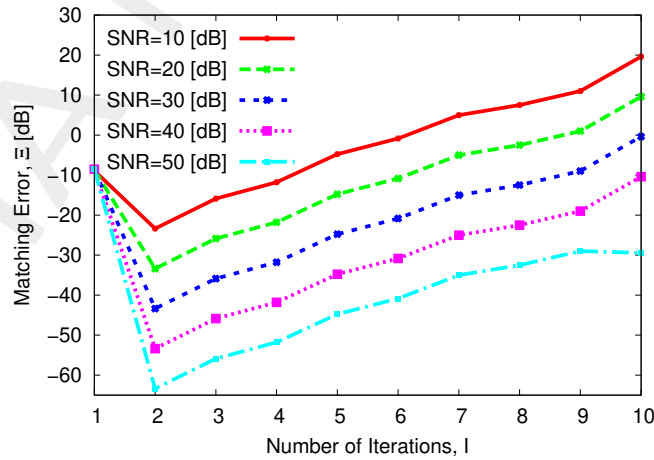


Figure 12: Behaviour of the near-field matching error versus the number of *OMP* iterations, I .

1.2.1 Comparison between original (*OMP*) and alternative (*BCS*) MbD

Near-Field Error

The comparison, in terms of near field error, between the original (*OMP*) and the alternative (*BCS*) MbD is reported in the following Fig. 13.

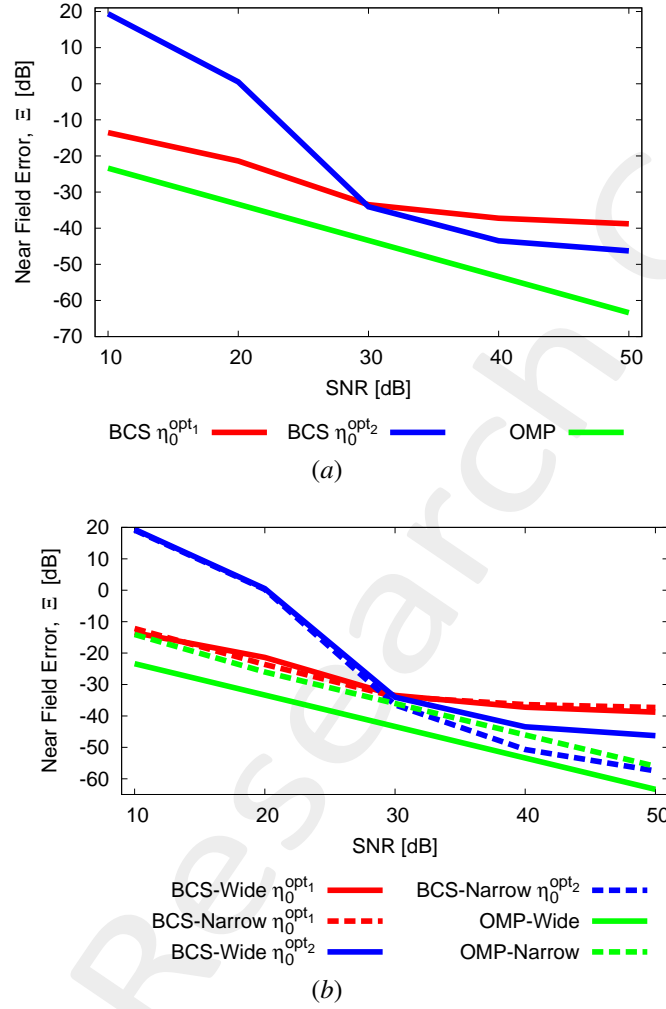


Figure 13: (a) Near Field Error comparison between original (*OMP*) and alternative (*BCS*) MbD for different *SNR* values and (b) comparison between the results

<i>SNR</i> [dB]	Near Field Error, Ξ [dB]		
	<i>BCS</i>		<i>OMP</i>
	η_0^{opt1}	η_0^{opt2}	
50	-38.79	-46.28	-63.37
40	-37.23	-43.47	-53.37
30	-33.47	-34.04	-43.37
20	-21.38	0.51	-33.37
10	-13.53	19.36	-23.37

Table IV: Near Field Errors obtained by the original (*OMP*) and alternative (*BCS*) MbD

Observations

Considering Fig. 13 (a):

-
- In this test case, the *OMP* algorithm outperforms the *BCS* solver whatever the *SNR* value, achieving an error $\Xi < -20$ [dB] even for the lower considered *SNR* value, $SNR = 10$ [dB];
 - About the *BCS* algorithm:
 - using η_0^{opt1} , the *BCS* solver obtains an error that is more or less 10 [dB] higher than that of the *OMP* algorithm for $SNR \leq 30$ [dB] and 20 – 30 [dB] higher for $SNR > 30$ [dB]. However, this *BCS* version performs highly better than the other one until $SNR = 30$ [dB] and then the results are comparable;
 - using η_0^{opt2} , the *BCS* algorithm obtains results which are the worst for $SNR \leq 30$ [dB] and a little bit better than the other *BCS* version, but always worse than those of the *OMP* algorithm.

Considering Fig. 13 (b):

- The increase of the failure ranges to build the over-complete basis does not have a great impact on the results; in particular:
 - the *OMP* presents a performance improvement of about 7 [dB] with respect to the same test case without enlarged ranges;
 - The *BCS* achieves the same result when η_0^{opt1} is used and slightly (~ 8 [dB]) worse results for $SNR \geq 40$ [dB] when η_0^{opt2} is used.

Estimated Near-Field

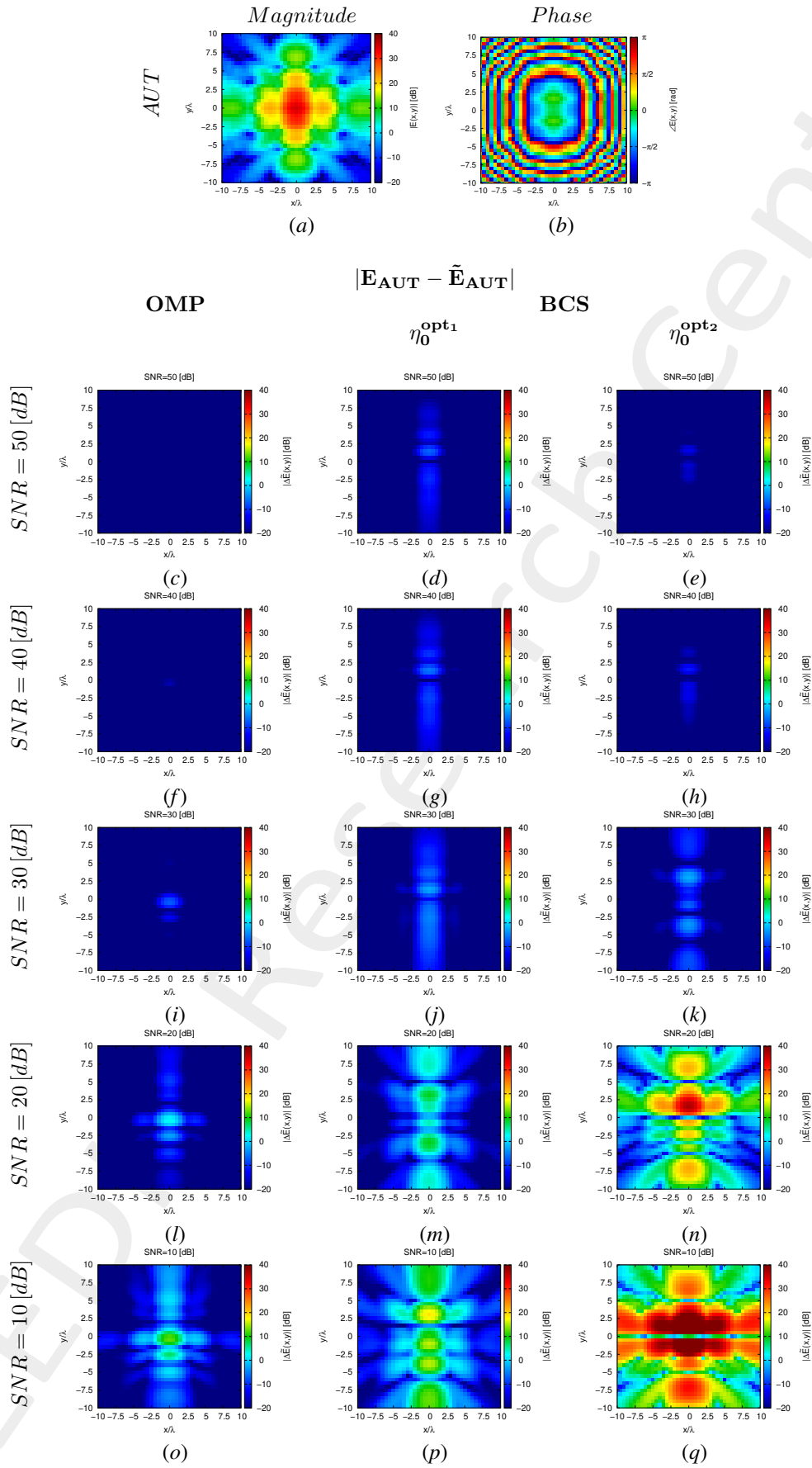


Figure 14: Magnitude difference between the actual and estimated 2 - D near-field pattern when processing noisy measurements at different SNRs.

Estimated Coefficients

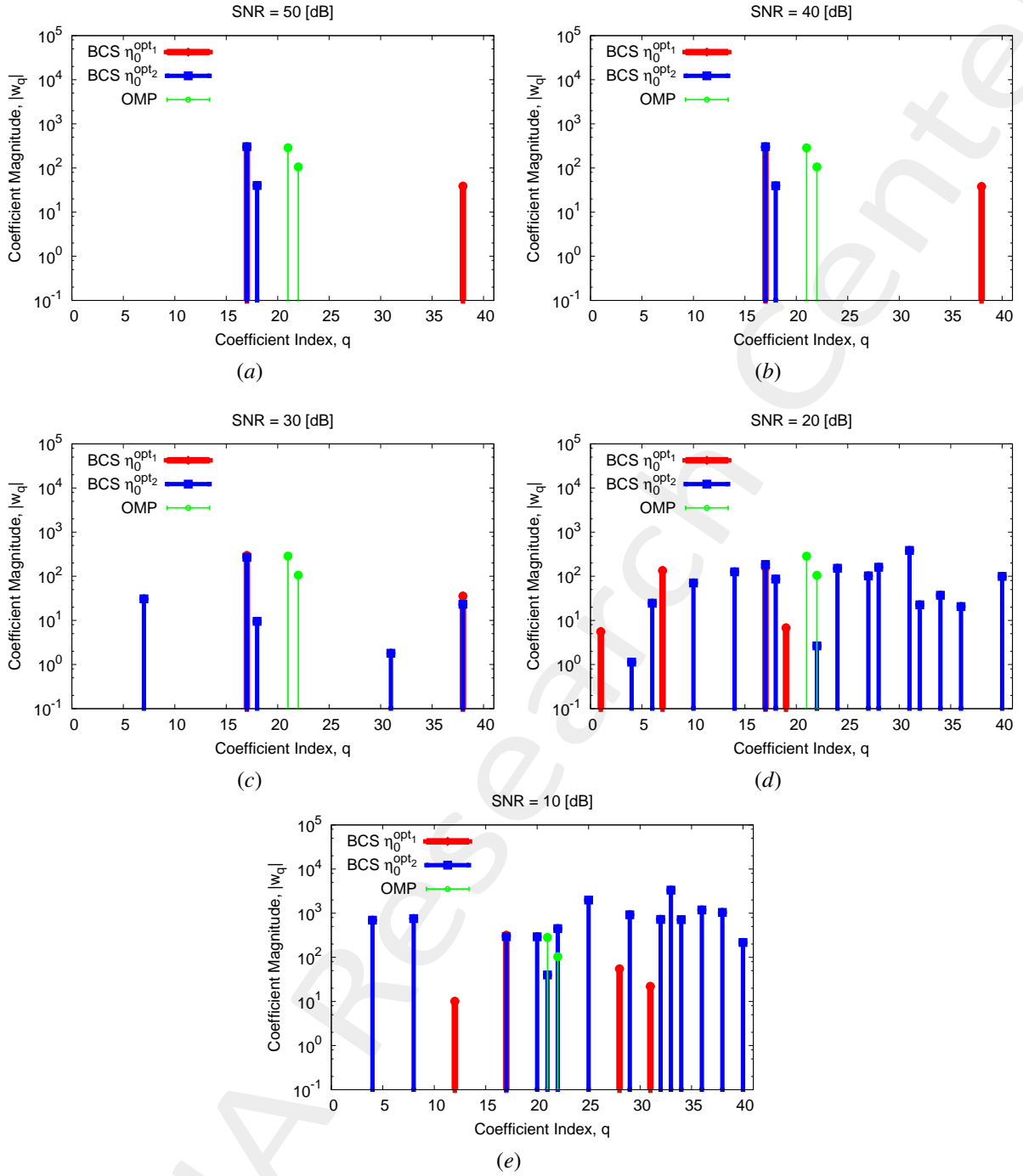


Figure 15: Coefficient comparison between original (*OMP*) and alternative (*BCS*) MbD : (a) $SNR = 50$ [dB], (b) $SNR = 40$ [dB], (c) $SNR = 30$ [dB], (d) $SNR = 20$ [dB], (e) $SNR = 10$ [dB]

Observations

- The *OMP* solver selects always the same vectors (vector indexes $q = 21, 22$), independently from the SNR value, which are related to phase failures and different from those selected by the *BCS* algorithm;
- The *BCS* algorithm presents solutions that are not sparse for low SNR values, $SNR = 20$ [dB] and $SNR = 10$ [dB], when η_0^{opt2} is used. Both the two *BCS* versions select always a same vector (vector index $q = 17$), but the overall vector selection is different.

1.2.2 OMP vs best BCS

The main idea of this section is to compare the performance of the *OMP* algorithm and the best *BCS* configuration.

Near-Field Error

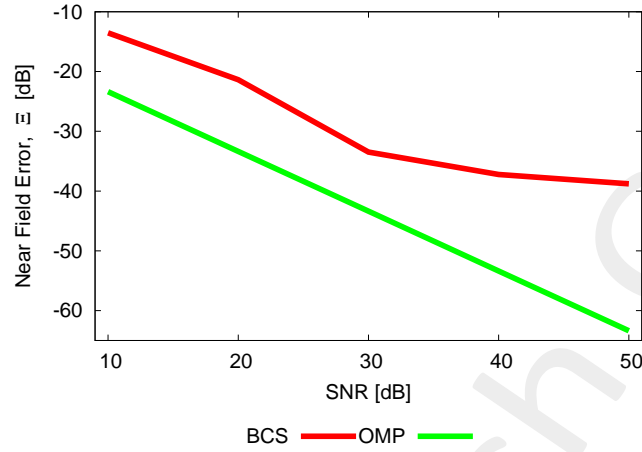


Figure 16: Near Field Error comparison between original (*OMP*) and alternative (*BCS*) MbD for different *SNR* values.

<i>SNR</i> [dB]	Near Field Error, Ξ [dB]	
	<i>BCS</i>	<i>OMP</i>
50	-38.79	-63.37
40	-37.23	-53.37
30	-33.47	-43.37
20	-21.38	-33.37
10	-13.53	-23.37

Table V: Near Field Errors obtained by the original (*OMP*) and alternative (*BCS*) MbD

Estimated Far-Field

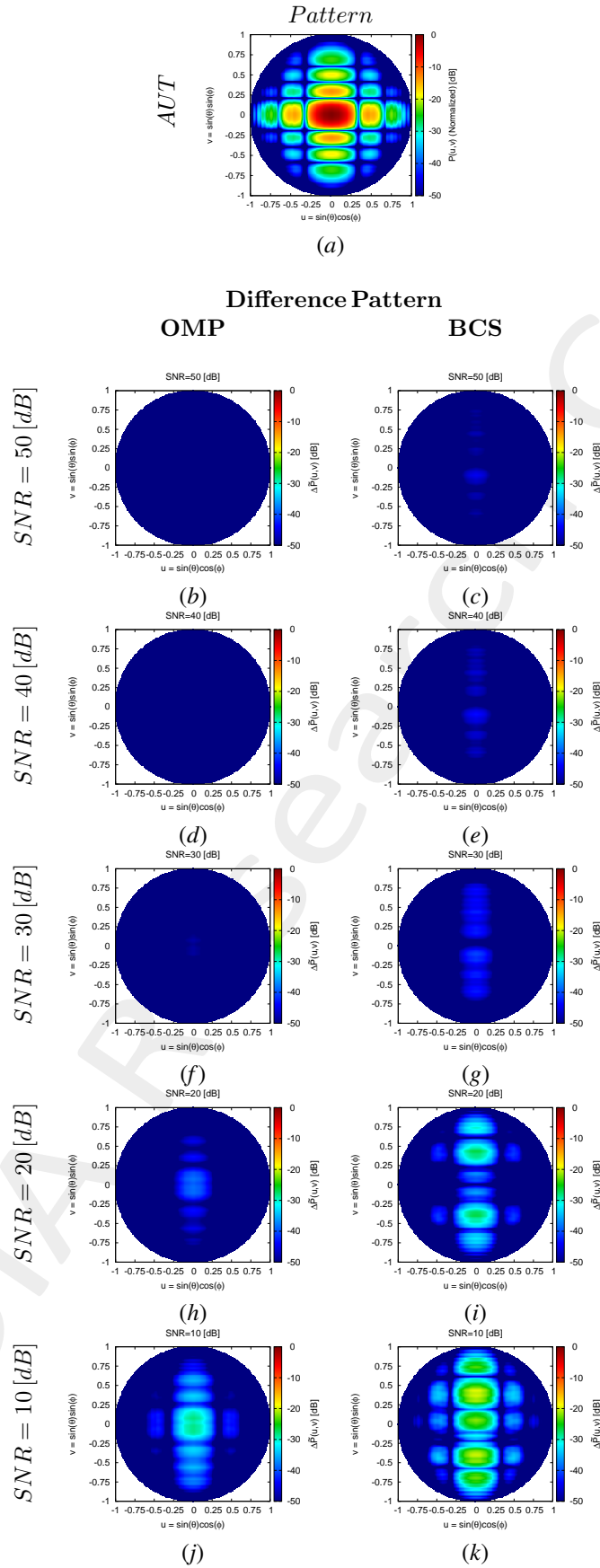


Figure 17: Difference between the actual and estimated 2 – D far-field pattern when processing noisy measurements at different $SNRs$.

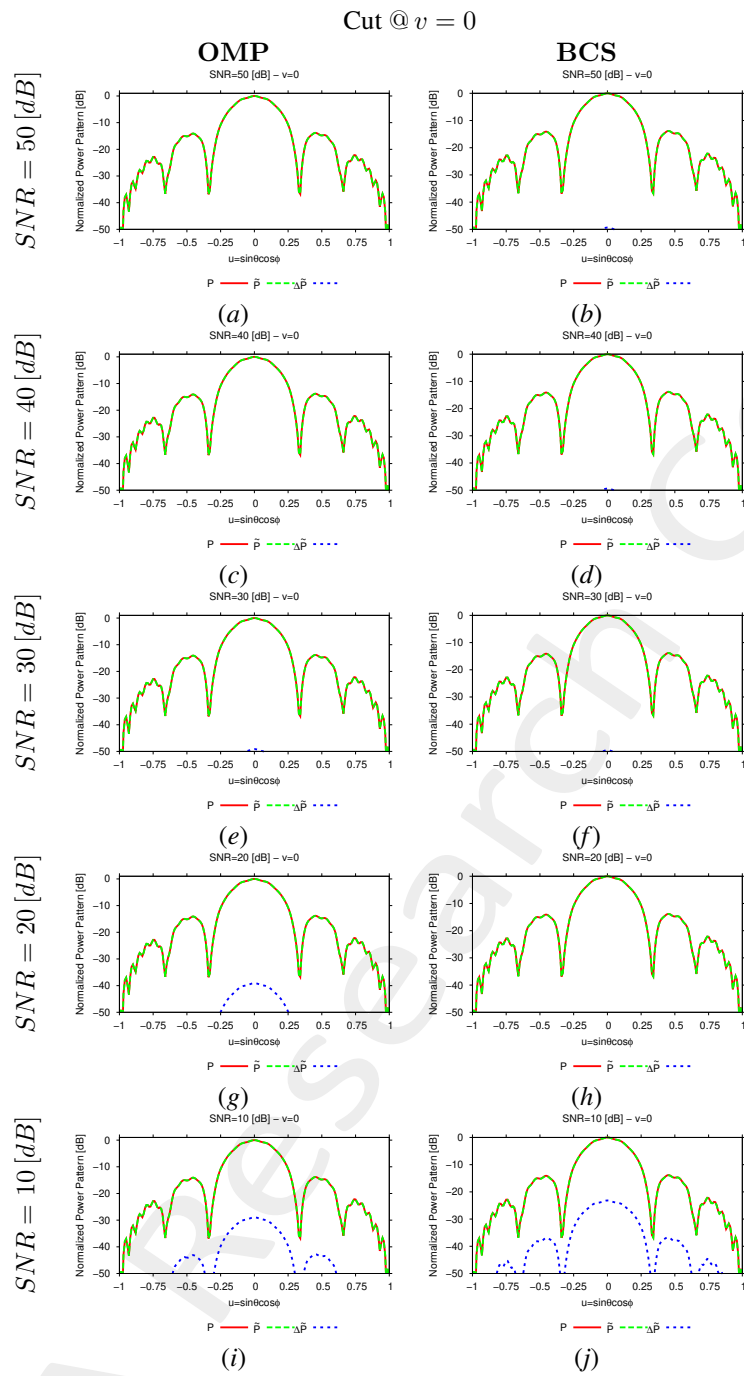


Figure 18: $1 - D$ cuts of the estimated far-field pattern (obtained through near-to-far-field transformation from the estimated near-field patterns) under several noisy conditions

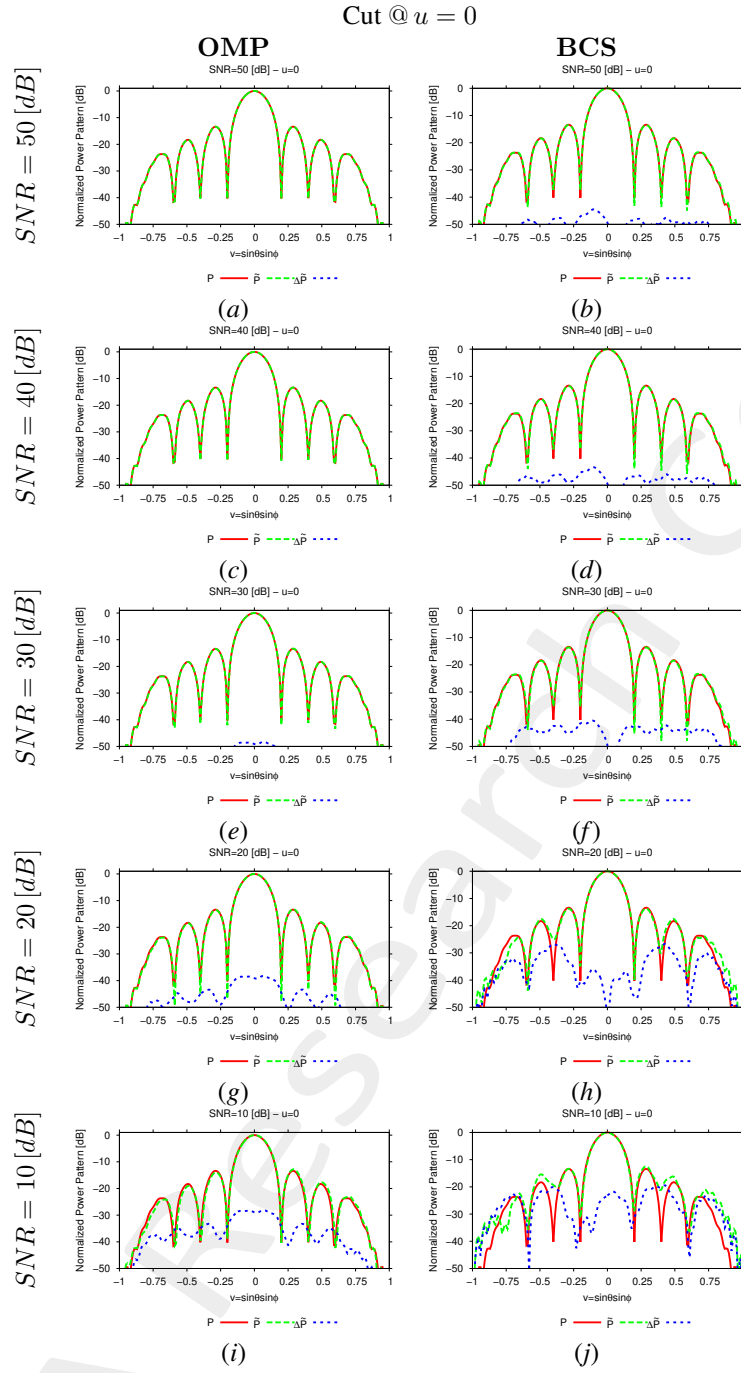


Figure 19: 1 – D cuts of the estimated far-field pattern (obtained through near-to-far-field transformation from the estimated near-field patterns) under several noisy conditions

SNR [dB]	Far – Field Error, χ [dB]	
	BCS	OMP
50	-39.86	-64.36
40	-38.35	-54.36
30	-34.70	-44.34
20	-22.90	-34.30
10	-14.86	-24.18

Table VI: Far-field matching error between the actual and estimated AUT patterns (both obtained through near-to-far-field transformation from the corresponding near-field patterns) under several noisy conditions.

Estimated Coefficients

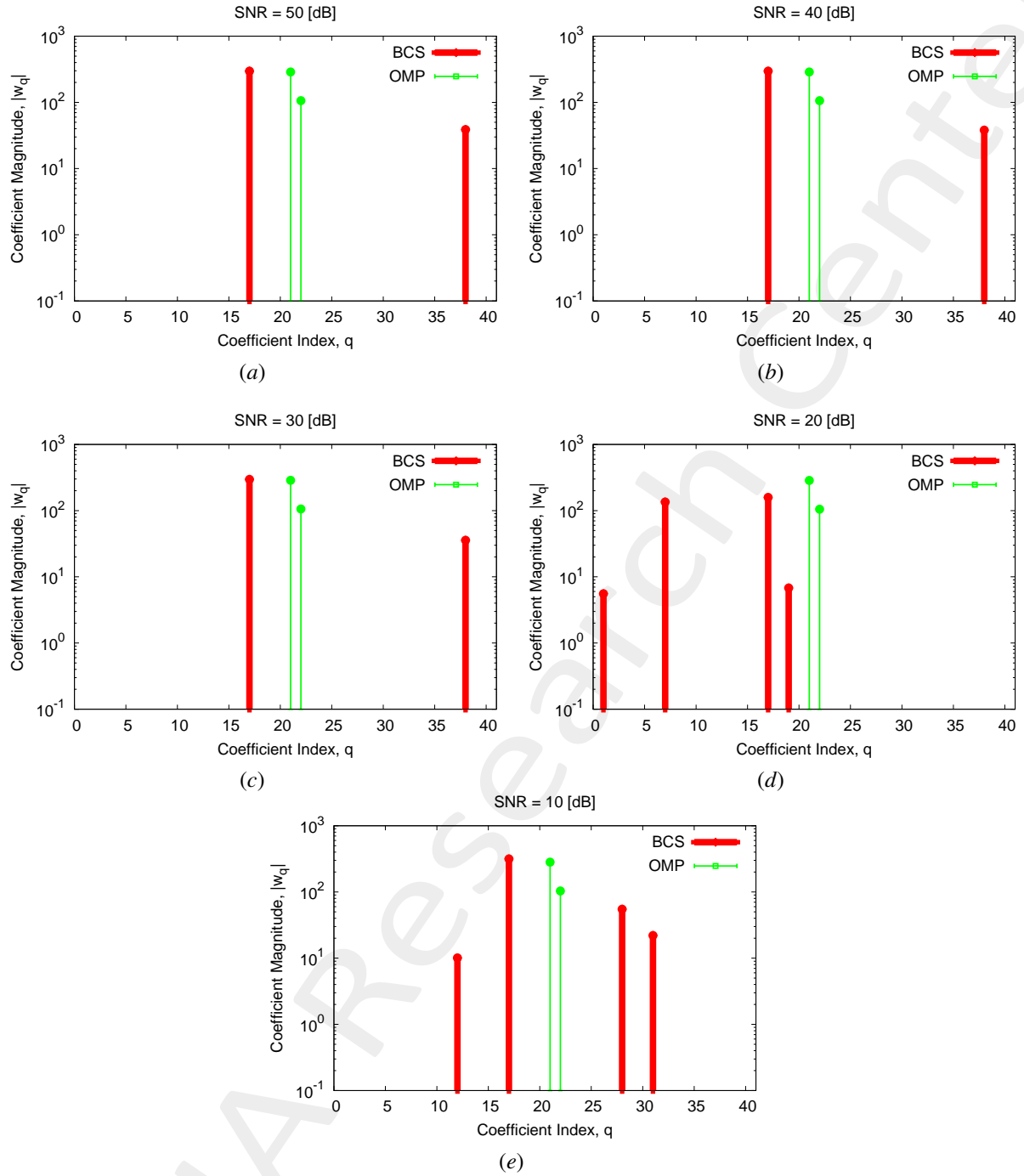


Figure 20: Coefficient comparison between original (*OMP*) and alternative (*BCS*) MbD: (a) $SNR = 50$ [dB], (b) $SNR = 40$ [dB], (c) $SNR = 30$ [dB], (d) $SNR = 20$ [dB], (e) $SNR = 10$ [dB]

More information on the topics of this document can be found in the following list of references.

References

- [1] M. Salucci, N. Anselmi, M. D. Migliore and A. Massa, "A bayesian compressive sensing approach to robust near-field antenna characterization," *IEEE Trans. Antennas Propag.*, vol. 70, no. 9, pp. 8671-8676, Sep. 2022 (DOI: 10.1109/TAP.2022.3177528).
- [2] B. Li, M. Salucci, W. Tang, and P. Rocca, "Reliable field strength prediction through an adaptive total-variation CS technique," *IEEE Antennas Wirel. Propag. Lett.*, vol. 19, no. 9, pp. 1566-1570, Sep. 2020.
- [3] M. Salucci, M. D. Migliore, P. Rocca, A. Polo, and A. Massa, "Reliable antenna measurements in a near-field cylindrical setup with a sparsity promoting approach," *IEEE Trans. Antennas Propag.*, vol. 68, no. 5, pp. 4143-4148, May 2020.
- [4] G. Oliveri, M. Salucci, N. Anselmi, and A. Massa, "Compressive sensing as applied to inverse problems for imaging: theory, applications, current trends, and open challenges," *IEEE Antennas Propag. Mag. - Special Issue on "Electromagnetic Inverse Problems for Sensing and Imaging,"* vol. 59, no. 5, pp. 34-46, Oct. 2017.
- [5] A. Massa, P. Rocca, and G. Oliveri, "Compressive sensing in electromagnetics - A review," *IEEE Antennas Propag. Mag.*, pp. 224-238, vol. 57, no. 1, Feb. 2015.
- [6] A. Massa and F. Teixeira, "Guest-Editorial: Special Cluster on Compressive Sensing as Applied to Electromagnetics," *IEEE Antennas Wirel. Propag. Lett.*, vol. 14, pp. 1022-1026, 2015.
- [7] G. Oliveri, N. Anselmi, M. Salucci, L. Poli, and A. Massa, "Compressive sampling-based scattering data acquisition in microwave imaging," *J. Electromagn. Waves Appl.*, vol. 37, no. 5, pp. 693-729, March 2023 (DOI: 10.1080/09205071.2023.2188263).
- [8] G. Oliveri, L. Poli, N. Anselmi, M. Salucci, and A. Massa, "Compressive sensing-based Born iterative method for tomographic imaging," *IEEE Trans. Microw. Theory Techn.*, vol. 67, no. 5, pp. 1753-1765, May 2019.
- [9] M. Salucci, L. Poli, and G. Oliveri, "Full-vectorial 3D microwave imaging of sparse scatterers through a multi-task Bayesian compressive sensing approach," *J. Imaging*, vol. 5, no. 1, pp. 1-24, Jan. 2019.
- [10] M. Salucci, A. Gelmini, L. Poli, G. Oliveri, and A. Massa, "Progressive compressive sensing for exploiting frequency-diversity in GPR imaging," *J. Electromagn. Waves Appl.*, vol. 32, no. 9, pp. 1164-1193, 2018.
- [11] N. Anselmi, L. Poli, G. Oliveri, and A. Massa, "Iterative multi-resolution bayesian CS for microwave imaging," *IEEE Trans. Antennas Propag.*, vol. 66, no. 7, pp. 3665-3677, Jul. 2018.
- [12] N. Anselmi, G. Oliveri, M. A. Hannan, M. Salucci, and A. Massa, "Color compressive sensing imaging of arbitrary-shaped scatterers," *IEEE Trans. Microw. Theory Techn.*, vol. 65, no. 6, pp. 1986-1999, Jun. 2017.

-
- [13] N. Anselmi, G. Oliveri, M. Salucci, and A. Massa, "Wavelet-based compressive imaging of sparse targets" *IEEE Trans. Antennas Propag.*, vol. 63, no. 11, pp. 4889-4900, Nov. 2015.
- [14] G. Oliveri, P.-P. Ding, and L. Poli, "3D crack detection in anisotropic layered media through a sparseness-regularized solver," *IEEE Antennas Wirel. Propag. Lett.*, vol. 14, pp. 1031-1034, 2015.
- [15] L. Poli, G. Oliveri, P.-P. Ding, T. Moriyama, and A. Massa, "Multifrequency Bayesian compressive sensing methods for microwave imaging," *J. Opt. Soc. Am. A*, vol. 31, no. 11, pp. 2415-2428, 2014.
- [16] G. Oliveri, N. Anselmi, and A. Massa, "Compressive sensing imaging of non-sparse 2D scatterers by a total-variation approach within the Born approximation," *IEEE Trans. Antennas Propag.*, vol. 62, no. 10, pp. 5157-5170, Oct. 2014.
- [17] L. Poli, G. Oliveri, F. Viani, and A. Massa, "MT-BCS-based microwave imaging approach through minimum-norm current expansion," *IEEE Trans. Antennas Propag.*, vol. 61, no. 9, pp. 4722-4732, Sep. 2013.
- [18] F. Viani, L. Poli, G. Oliveri, F. Robol, and A. Massa, "Sparse scatterers imaging through approximated multitask compressive sensing strategies," *Microwave Opt. Technol. Lett.*, vol. 55, no. 7, pp. 1553-1558, Jul. 2013.
- [19] L. Poli, G. Oliveri, P. Rocca, and A. Massa, "Bayesian compressive sensing approaches for the reconstruction of two-dimensional sparse scatterers under TE illumination," *IEEE Trans. Geosci. Remote Sensing*, vol. 51, no. 5, pp. 2920-2936, May 2013.
- [20] P. Rocca, N. Anselmi, M. A. Hannan, and A. Massa, "Conical frustum multi-beam phased arrays for air traffic control radars," *Sensors*, vol. 22, no. 19, 7309, pp. 1-18, 2022 (DOI: 10.3390/s22197309)
- [21] F. Zardi, G. Oliveri, M. Salucci, and A. Massa, "Minimum-complexity failure correction in linear arrays via compressive processing," *IEEE Trans. Antennas Propag.*, vol. 69, no. 8, pp. 4504-4516, Aug. 2021.
- [22] N. Anselmi, G. Gottardi, G. Oliveri, and A. Massa, "A total-variation sparseness-promoting method for the synthesis of contiguously clustered linear architectures," *IEEE Trans. Antennas Propag.*, vol. 67, no. 7, pp. 4589-4601, Jul. 2019.
- [23] M. Salucci, A. Gelmini, G. Oliveri, and A. Massa, "Planar arrays diagnosis by means of an advanced Bayesian compressive processing," *IEEE Trans. Antennas Propag.*, vol. 66, no. 11, pp. 5892-5906, Nov. 2018.
- [24] L. Poli, G. Oliveri, P. Rocca, M. Salucci, and A. Massa, "Long-Distance WPT Unconventional Arrays Synthesis," *J. Electromagn. Waves Appl.*, vol. 31, no. 14, pp. 1399-1420, Jul. 2017.
- [25] G. Oliveri, M. Salucci, and A. Massa, "Synthesis of modular contiguously clustered linear arrays through a sparseness-regularized solver," *IEEE Trans. Antennas Propag.*, vol. 64, no. 10, pp. 4277-4287, Oct. 2016.
- [26] M. Carlin, G. Oliveri, and A. Massa, "Hybrid BCS-deterministic approach for sparse concentric ring isophoric arrays," *IEEE Trans. Antennas Propag.*, vol. 63, no. 1, pp. 378-383, Jan. 2015.
- [27] G. Oliveri, E. T. Bekele, F. Robol, and A. Massa, "Sparsening conformal arrays through a versatile BCS-based method," *IEEE Trans. Antennas Propag.*, vol. 62, no. 4, pp. 1681-1689, Apr. 2014.
-

-
- [28] F. Viani, G. Oliveri, and A. Massa, "Compressive sensing pattern matching techniques for synthesizing planar sparse arrays," *IEEE Trans. Antennas Propag.*, vol. 61, no. 9, pp. 4577-4587, Sept. 2013.
- [29] P. Rocca, M. A. Hannan, M. Salucci, and A. Massa, "Single-snapshot DoA estimation in array antennas with mutual coupling through a multi-scaling BCS strategy," *IEEE Trans. Antennas Propag.*, vol. 65, no. 6, pp. 3203-3213, Jun. 2017.
- [30] M. Carlin, P. Rocca, G. Oliveri, F. Viani, and A. Massa, "Directions-of-arrival estimation through Bayesian Compressive Sensing strategies," *IEEE Trans. Antennas Propag.*, vol. 61, no. 7, pp. 3828-3838, Jul. 2013.
- [31] M. Carlin, P. Rocca, G. Oliveri, and A. Massa, "Bayesian compressive sensing as applied to directions-of-arrival estimation in planar arrays," *J. Electromagn. Waves Appl.*, vol. 2013, pp. 1-12, 2013 (DOI :10.1155/2013/245867).